Optics Communications 448 (2019) 1–9

Contents lists available at ScienceDirect

Optics Communications

journal homepage: www.elsevier.com/locate/optcom

Ultra-broadband and high absorbance metamaterial absorber in long wavelength Infrared based on hybridization of embedded cavity modes

Yi Luo [a,b], Zhongzhu Liang [a,*], Dejia Meng [a], Jin Tao [a], Jingqiu Liang [a], Changhong Chen [c], Jianjun Lai [c], Yuxin Qin [a], Jinguang LV [a], Yuhao Zhang [a,b]

[a] State Key Laboratory of Applied Optics, Changchun Institute of Optics, Fine Mechanics and Physics, Chinese Academy of Sciences, Changchun, 130033, China
[b] University of the Chinese Academy of Sciences, China
[c] Wuhan National Laboratory for Optoelectronics, Huazhong University of Science and Technology, Wuhan 430074, China

ARTICLE INFO

Keywords:
Metamaterial absorbers
Long wavelength infrared
Embedded cavity modes

ABSTRACT

We present a novel ultra-broadband, polarization-independent, and wide-angle metamaterial absorber whose metal–insulator–metal cavities are embedded into bulk insulator nanodisks. The hybridization of multiple embedded cavity modes generated by the combination of dielectric-loaded surface plasmon polaritons waveguide and cavity modes contributes to large bandwidth and high absorption in the long wavelength infrared (LWIR) region. The proposed structure exhibits more than 94% absorbance in the interval from 8 μm to 16 μm; and more than 95% absorbance over the whole LWIR band (8–14 μm), which is superior than the initial MIM structure (absorption greater than 90% from 8.10–14.33 μm) and similar kinds of metamaterial absorber based on noble metal. In addition, a nearly perfect absorbance (more than 99%) is obtained in the 11.22–12.46 μm and 13.26–14.59 μm wavebands. Moreover, results show that the resonant wavelength and operating bandwidth can be adjusted flexibly by varying related geometry parameters. Thus, the wavelength-selective metamaterial absorber is promising for thermal emitters, energy harvester and microbolometers.

1. Introduction

Plasmonic metamaterial absorbers have risen wide spread attention due to their extraordinary electromagnetic property in many unprecedented applications such as microbolometers [1,2], super lenses [3], thermal emitters [4,5], energy harvester [6–9], and chemical sensing [10]. Unlike traditional absorbers determined by their intrinsic absorbing properties, plasmonic metamaterial absorbers can realize the impedance matching to that of free space by designing the artificial "meta-atoms". Due to the unique optical characteristics of strong localized field enhancement and near-perfect absorption, various methods for designing metamaterial absorbers appear an endless stream. The first experimental metamaterial perfect absorber in the microwave regime was proposed by Landy et al. in 2008 [11]. Subsequently, the electromagnetic response-based method is widely applied in the terahertz (THz) metamaterial absorbers [12]. While for infrared (IR) region, due to the plasma resonance of metal in high frequency region, the typical metamaterial absorber is a periodic array of metal–insulator–metal (MIM) resonator units which depends on the coupling of incident light with surface plasmon resonance generated by the MIM resonator [13–15]. During the last decade, metamaterial absorbers, working in the IR spectral range, has continuously evolved due to the explosion development of microbolometer [16–18].

Plasmonic metamaterial absorbers often suffer from a narrow wavelength bandwidth because their absorption originates in electric and magnetic resonances. It considerably limits the application of the metamaterial absorbers in various fields where broadband or multiband absorption is in demand. A series of methods to expand the absorption bandwidth have been proposed. A common strategy is to mix multiple resonators in the same horizontal plane [19,20]. However, it is difficult to control the distance between adjacent resonators and sub-wavelength size. Another approach is to accumulate multiple resonators on the vertical surface [21,22], but the designs are not appropriate to the compact structure because of the large thickness. Besides, algorithms can be used to produce the broadband super-cell units [23,24], but this method occurs complex iterations and fabrication. Recently, a novel ultrathin absorber design based on embedded insulator–metal–insulator has been verified [25]. The broadband absorption is achieved in visible to near-infrared regime by the excitation of both surface plasmon resonance (SPR) and localized SPR. In spite of these achievements, the broadband absorption with high absorption efficiency of the metamaterial absorbers operating in long-wavelength infrared (LWIR) atmospheric windows (8–14 μm wavelength) are rarely reported. Furthermore, in LWIR band, the material and shape of absorbers are need to be adjusted for broadband absorption with high absorption efficiency.

* Corresponding author.
E-mail address: liangzz@ciomp.ac.cn (Z. Liang).

https://doi.org/10.1016/j.optcom.2019.04.080
Received 12 March 2019; Received in revised form 15 April 2019; Accepted 29 April 2019
Available online 10 May 2019
0030-4018/

Inspired by previous research on broadening the bandwidth of plasmonic metamaterial absorbers, we have proposed a broadband absorber design which exhibits excellent absorption within the entire LWIR band. We employed a bulk insulator nanodisk in substitution for the air medium so that the traditional MIM structure is immersed within a large insulator nanodisk. It is realized based on the excitation of multiple embedded cavity modes generated by the combination of dielectric-loaded surface plasmon polaritons waveguide and cavity modes. The superiority of the embedded structure is numerically investigated by comparing the physical mechanism and the geometry effects of the two metamaterial absorbers. The modified embedded structure appears to exhibit an average absorptivity greater than 94% from 8.00 μm to 16.00 μm (greater than 95% absorbance in the 8–14 μm waveband), which represents better performance than the initial traditional MIM structure (absorption greater than 90% from 8.10–14.33 μm). Moreover, the wavelength-selective metamaterial absorber is realized by controlling the related geometry parameters. This work provides the reference for the design of tunable broadband LWIR absorbers. It is manifest that this design method can be extended to medium wavelength infrared, very long-wavelength infrared, terahertz, or visible regimes. Furthermore, this absorber structure with MEMS-COMOS technology compatibility will hold considerable potential in thermal emitters, microbolometer, energy harvester, and chemical sensing applications.

The paper is developed according to the following structure: In Section 2, we present our initial absorber design and numerically investigated the physical mechanism and geometrical effect. In Section 3, we modify our structure to further improve the absorption performance by incorporating different resonance modes from the embedded metal–insulator layer. Similarly, we numerically investigated the physical mechanism and geometrical effect. Finally, conclusions are drawn in Section 4.

2. Design and analysis of ultra-broadband metamaterial absorber

2.1. Ultra-broadband plasmonic absorber structure

The initial metamaterial absorber is designed as a metal–insulator–metal (MIM) structure where the upper three layers are patterned. The structure is given in Figs. 1(a) and 1(b). The absorber design consists of a thick continuous Ti bottom layer, followed by a planar Ge layer, the third layer of Ti nanodisk patterns, then another layer of Ge nanodisk patterns, and the last layer is Ti nanodisk patterns. The possible top layer structures for periodic micropatches are square patches and circulars. Generally, the top layer structures have less impact on absorption properties because of the common resonant modes. In this article, we choose the circular top layer as an example to design the broadband absorber. The absorption capability of the MIM absorber can be described by the effective medium theory [26,27]. If the effective impedance of the absorber is perfectly matched with free space, the reflection will be reduced at matching points. And the effective impedance can be defined as follows:

$$Z(w) = \sqrt{\frac{\mu(w)}{\varepsilon(w)}} = \sqrt{\frac{\left(1+S_{11}(w)\right)^2 - S_{21}(w)^2}{\left(1-S_{11}(w)\right)^2 - S_{21}(w)^2}} \tag{1}$$

where, $\varepsilon(w)$ is the electric permittivity of the structure, and $\mu(w)$ is the magnetic permeability. $S_{11}(w)$ and $S_{21}(w)$ are the real part and imaginary part of reflection coefficient and transmission coefficient, respectively. The relationship between the reflection coefficient and equivalent impedance can be described by:

$$R(w) = \left|S_{11}(w)\right|^2 = \left|\frac{Z(w) - Z_0}{Z(w) + Z_0}\right|^2 \tag{2}$$

with Z_0 being the impedance of free space. Thus, this arrangement promotes the coupling effects of free space electromagnetic waves in the infrared region to insulator layer. The reason behind this is that the nanodisk insulator layer and the free space around the insulator join together to form an effective medium, which makes the reflection constant in this medium smaller than that in the free space and a planar insulator [28]. As a result, the absorber can reflect less electromagnetic power to the surrounding region leading to higher absorption.

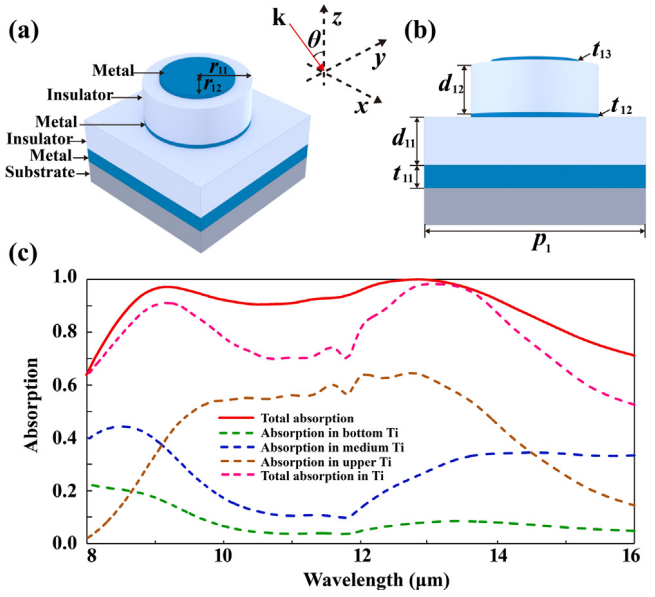

Fig. 1. Schematic illustration and simulation of the metamaterial absorber (a) 3-D view. (b) side view. (c) Total absorption and absorption ability in different Ti metal layers of the proposed absorber.

The structure and parameters are analysed and optimized by numerical parameter sweep based on finite difference time domain method. The radius (r) of the lower and upper Ti nanodisk patterns are r_{11} = 0.80 μm and r_{12} = 0.55 μm, respectively. The radius of the Ge nanodisk patterns is in consistent with the lower Ti nanodisk. The thicknesses (t) of the Ti metallic layers from bottom to top are t_{11} = 0.25 μm, t_{12} = 0.025 μm, and t_{13} = 0.025 μm. The thicknesses of the planar Ge layer and Ge nanodisk are d_{11} = 0.52 μm and d_{12} = 0.60 μm, respectively. The repeat period (p_1) of the unit cell is 2.4 μm. Herein, Titanium (Ti) is selected as the metallic material because of its lossy behaviour in the IR region. Germanium (Ge) is employed as the lossless dielectric material due to its transparent behaviour in the long wavelength infrared. The complex dielectric constants of Ti and Ge are modelled by a Drude–Lorentz fitting to tabulate the experimental data [29]. The thickness of the bottom metal functional layer is considerably larger than the skin thickness of electromagnetic waves in the long wavelength infrared and will inhibit any incident light transmitted through the multilayer structure, leading to nearly zero transmission in the target band. A thinner Ti metal layer is employed to guarantee sufficient coupling effects. Finite difference time domain (FDTD) method has been used to simulate the field distributions of ultra-broadband absorber. In the FDTD numerical simulations, the periodical boundary conditions are adopted in the x and y directions, and the perfectly matching layers (PML) are employed in the z direction. Absorption (A) is usually calculated by the formula $A = 1 - R - T$, where R and T represent reflection and transmission. Transmission equals zero since the thickness of the bottom metal layer is much larger than its skin depth to eliminate transmission, which indicates that $A = 1 - R$.

The total absorption spectrum is split into individual absorption spectra of different Ti metal layers due to the highly lossy Ti. Absorption changes over the wavelength function plot are given in Fig. 1(c), which shows that the structure has an average absorptivity that is greater than 90% in the wavelength interval between 8.10 μm and

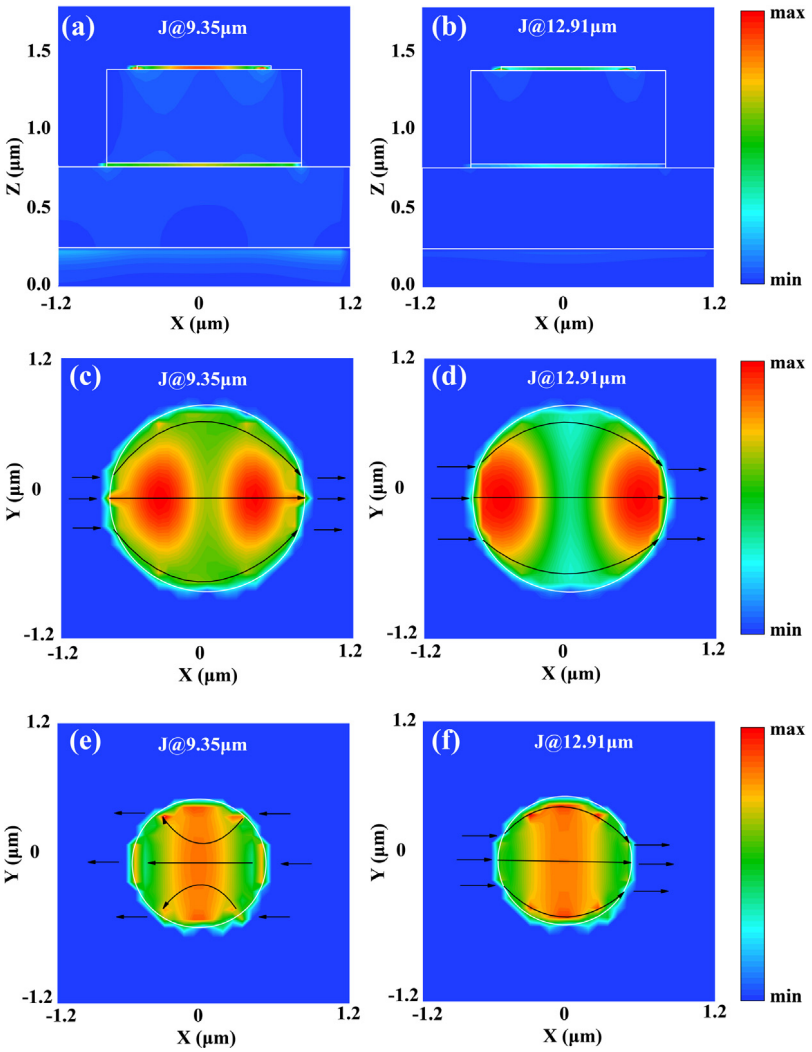

Fig. 2. (a)–(b) current density distributions (colour bar in the x-z plane) at different resonant wavelengths. (c)–(d) Surface current distributions in lower Ti nanodisk (colour bar in the x-y plane) at different resonant wavelengths. (e)–(f) Surface current distributions in upper Ti nanodisk (colour bar in the x-y plane) at different resonant wavelengths.

14.33 μm and greater than 99% absorbance in the 12.15–13.48 μm wavebands. Two absorption peaks (9.35 μm and 12.91 μm) arise in a separated location in the absorption spectrum. In addition, based on the presented model, the absorption in Ti metal layers is dominant all over the spectrum. This result implies that the energy loss in Ti results in broadband absorption. Ti, which is a highly lossy metal, helps to enhance the resistive effects, which in turn produces resonance with a relatively lower quality factor and effectively expands the operating bandwidth. Moreover, the role of the top metal layer is to bind the incident light to the insulator layer by the evanescent wave propagating through the top metal [30]. When the rigorous coupling condition that is related to the permittivity and thickness of the metal is satisfied, the incident light will be perfectly absorbed by excitation of the resonant cavity modes. Thus, the top metal determines the coupling strength between the incident light and the resonant cavity.

2.2. The mechanism of the broadband absorption of metamaterial absorber

To understand the resonance nature of the initial metamaterial absorber reported in this paper and the mechanism of the absorption, the current density of the proposed structure at each resonant wavelength are given in Fig. 2. As it seen from Figs. 2(a)–(b), electric current mainly distributes in upper and lower Ti nanodisks, indicating that energy loss is the cause of broadband absorption. The distributions of surface current at each resonant wavelength for the lower and upper layer are plotted in Figs. 2(c)–(d) and 2 (e)–(f), respectively. Overall, the distributions of surface current in the upper and lower layers are different, which means that the resonances in the upper and lower layers are also different. As shown in Figs. 2(c)–(d), for the lower thin Ti nanodisk layer, the surface currents widely distributed in the left and right region of the Ti nanodisk. While for the upper Ti nanodisk layer presented in Figs. 2(e)–(f), the surface currents are mainly concentrated on the top and bottom edges of the Ti nanodisk. For the short wavelength of 9.35 μm, the surface currents on the lower layer mainly flow along the direction of the arrows, and on the upper layer the surface currents are in the opposite direction. Thus, magnetic dipoles originate from the excited antiparallel currents in the upper and lower Ti nanodisk layers. For the long wavelength of 12.91 μm, electric dipoles are caused by the parallel currents between two Ti nanodisk layers. The magnetic and electric resonance couple with external electromagnetic fields and produces strong absorption phenomena at different resonance wavelengths [9].

To further explain the physical mechanism of the absorber, the electromagnetic field distributions at each resonant wavelength are investigated, as shown in Fig. 3. Fig. 3(a)–(b) present the electric field distributions of the x-z plane at different resonant frequencies. It can be seen from the figure that electric field is strongly confined mainly in the air-slot of the upper Ti nanodisk. The electric field distributions of the x-z plane imply that the surface plasmon polaritons (SPPs) are excited in the metamaterial absorber. Figs. 3(c)–(d) are the magnetic field

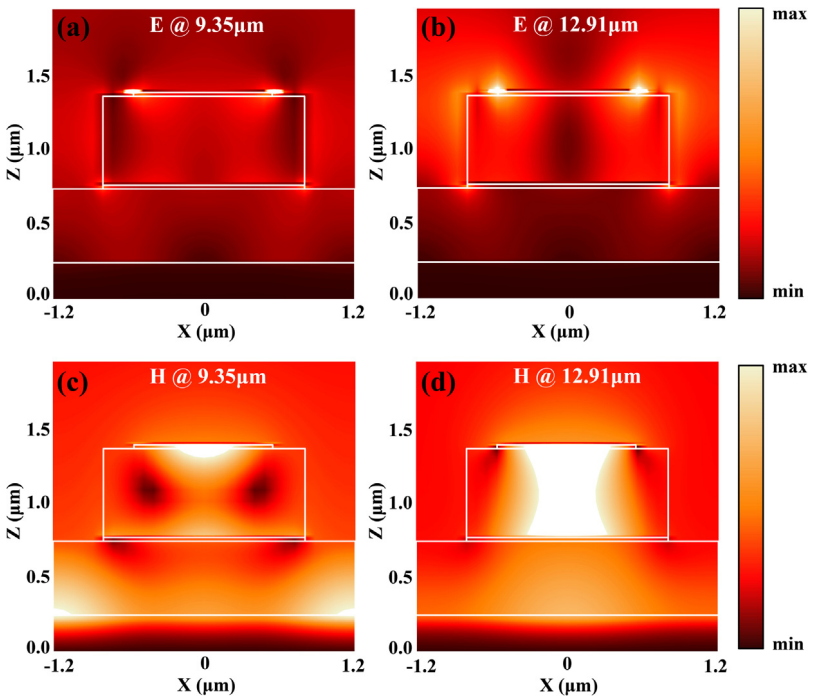

Fig. 3. (a)–(b) Electric field $|E|$ distributions (colour bar in the x-z plane) at different resonant wavelengths. (c)–(d) Magnetic field $|M|$ distributions (colour bar in the x-z plane) at different resonant wavelengths.

distributions of the x-z plane. Overall, two different resonant modes are observed from Figs. 3(c)–(d). In order to understand the mechanism of the absorption easily, the entire absorber can be regarded as two parts: The upper part of the absorber comprises two Ti nanodisks and an insulator layer in between. It forms a resonant cavity enclosed by magnetic walls that supports cavity mode. In an individual MIM resonator, multiple waves in the upper and lower metal–insulator interface reflected at the edges interfere with each other, and the destructive interference produces the cavity mode, which causes cavity mode-induced light absorption [31]; The lower part consists of a continuous metal substrate and a planar Ge layer, which supports propagating surface plasmon (PSP) mode between continuous Ti film and Ge spacer. With respect to the short wavelength of 9.35 μm, the magnetic field enhancement is considered to be the combination of the PSP mode generated at lower part and cavity mode generated at upper part, where the magnetic field is not only strongly confined in the gap region underneath the upper Ti nanodisk, but also intensively enhanced between the adjacent cells. With respect to the long wavelength of 12.91 μm, the magnetic field at resonance is greatly enhanced and confined in insulator Ge nanodisk, which indicates that the resonant cavity mode dominates the absorption.

2.3. Effects of geometry on absorption performance of metamaterial absorber

We next investigate the effect of some geometry parameters on the performance of this metamaterial absorber. In Fig. 4, we illustrate the important parameters that affect the performance of the initial structure. Figs. 4(a)–(d) show the absorption efficiency as a function of the thickness of the planar Ge layer (d_{11}), the thickness of the Ge nanodisk (d_{12}), and the radius of the lower and upper Ti nanodisk r_{11} and r_{12}, respectively. One can see from Fig. 4 that the resonant frequency of these two resonances can be tuned by adjusting the thickness of the insulator Ge layer and the radius of the Ti nanodisks. A comparison between Figs. 4(a) and 4(b) reveals that the PSP resonant wavelength takes on a remarkable redshift with increasing thickness of the planar Ge layer (d_{11}). However, the PSP resonant wavelength is less disturbed by the thickness of the Ge nanodisk (d_{12}). This can be explained by the fact that the energy of magnetic PSP is mostly confined in the lower planar Ge layer rather than the upper Ge nanodisk, and the phase change is enhanced with the increase of thickness of the dielectric, thus leading to the reduction of the PSP resonant wavelength to obtain the perfect interference condition at the Ge–air interface [32]. While for cavity mode, the resonant wavelength of cavity mode can be affected by the thickness of the Ge nanodisk (d_{12}), but exhibits less sensitivity to the thickness of the planar Ge layer (d_{11}). This is because the cavity mode originates from the constructive interference of coupled surface plasmons that is heavily influenced by the effective cavity length [33,34]. On the other hand, the cavity mode can be significantly affected by the radius of nano-disks, which is based on the interference of multiple waves scattered by upper and lower Ti nanodisks. As the radius of nanodisks increases, the MIM structure exhibits the tendency of a continuous sandwiched film, which causes a broader absorption bandwidth and lower average absorptivity [30]. Therefore, the cavity mode undergoes a marked redshift with increasing radius of nanodisks. Furthermore, the radius of nanodisks is a decisive factor which may determine the long wavelength limit of absorption bandwidth with the other parameters fixed.

3. Modified embedded metamaterial absorber

3.1. Modified embedded structure

It is possible to expand the bandwidth of the metamaterial absorber by embedding the MIM cavity into insulator layer. The adjoining embedded structure can effectively tune reflection amplitude and phase retardation, which plays an important role in the peak width and the position of the resonant peak. Moreover, the hybridization of various resonant modes in the operating band can be achieved by introducing the embedded metal–insulator layer, which offers a probability to enhance the bandwidth and absorption [25,34]. The modified structure is illustrated in Figs. 5(a) and 5(b), the upper three patterned layers are embedded into the insulator layer of a bulk Ge nanodisk so that the original insulator nanodisk is incorporated into the insulator layer

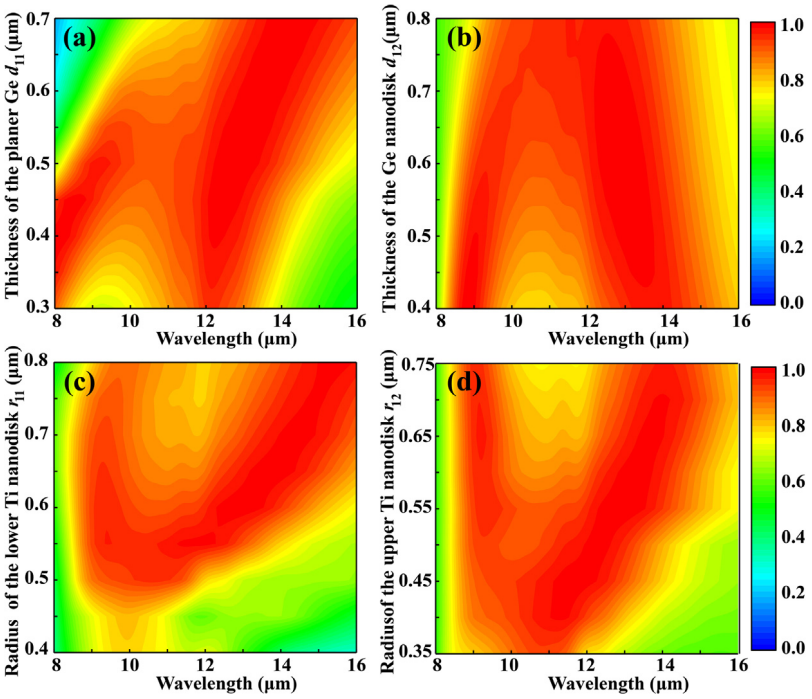

Fig. 4. Demonstration of the geometric effects on the absorption performances: (a) the thickness of the planar Ge layer (d_{11}), (b) the thickness of the Ge nanodisk (d_{12}), (c)–(d) the radius of the lower and upper Ti nanodisk r_{11} and r_{12}.

and the two metallic nanodisks are immersed in different levels within a large insulator nanodisk. A relatively better absorption performance of the embedded structure is possible to be achieved due to coupling from different resonant modes. With the numerical parameter sweep, the final optimal geometrical parameters are provided as follows: the period of the unit cell is p_2 = 1.97 μm; and the thicknesses of the Ti metallic layers from bottom to top are t_{21} = 0.25 μm, t_{22} = 0.05 μm, t_{23} = 0.035 μm, respectively. The lower and upper Ti nanodisk patterns and the bulk Ge nanodisk have different radius of r_{2i} (i = 1, 2, 3), including r_{21} = 0.50 μm, r_{22} = 0.30 μm, and r_{23} = 0.80 μm. The thickness of the planar Ge layer is d_{21} = 0.44 μm. The face-to-face distance between the two patterned metal layers is d_{22} = 0.25 μm, and the distance between the upper Ti nanodisk and the top of the bulk Ge nanodisk are d_{23} = 0.45 μm. The absorption ability spectrum of different Ti metal layers in the embedded structure is displayed in Fig. 5(c), including the bottom functional Ti layer, medium and upper metamaterial ring layers. In Fig. 5(c), as seen in total absorption spectrum, merged resonant peaks and more than 94% absorbance are observed in the interval from 8 μm to 16 μm; and more than 95% absorbance are observed in the interval from 8 μm to 14 μm. In addition, a nearly perfect absorbance (more than 99%) is obtained in the 11.22–12.46 μm and 13.26–14.59 μm wavebands. Three absorption peaks are located at the wavelengths λ_1 = 9.39 μm, λ_2 = 11.81 μm, and λ_3 = 14.17 μm in the absorption spectrum. Moreover, almost all the absorption occurs in the metamaterial ring layers, while moderately affected by the bottom metal. The absorption peak at 9.39 μm attributes to the lower metamaterial ring layer, while the absorption peak at 14.17 μm mainly originates from the upper metamaterial ring layer. On the other hand, the absorption peak at the middle wavelength range comes from the blending of discrete absorption peaks which come from inductive and/or capacitive mutual resonance effect between the upper metamaterial layer and lower metamaterial layer [35].

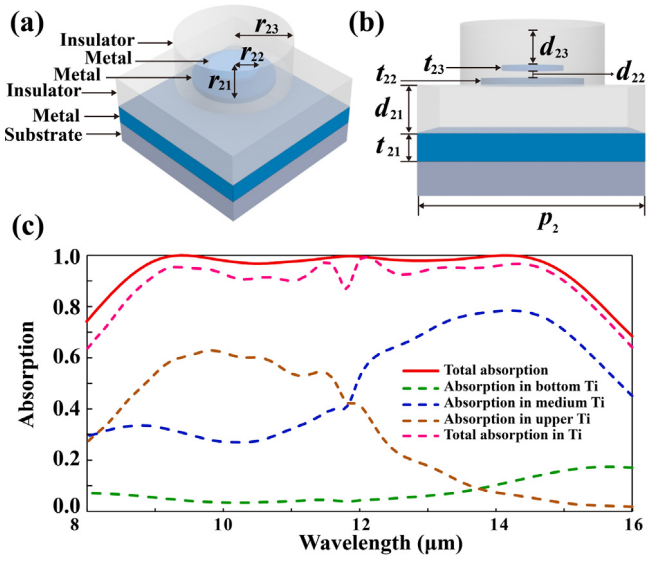

Fig. 5. Schematic illustration and simulation of the Modified embedded metamaterial absorber (a) 3-D view. (b) side view. (c) Total absorption and absorption ability in different Ti metamaterial ring layers of the proposed absorber.

3.2. The mechanism of the modified embedded metamaterial absorber

Similar results of the current density are presented in Fig. 6 for the modified embedded structure. As shown in Figs. 6(a)–(c), the response is very similar to the electric current distributions in Figs. 6(a)–(c), electric current mainly distributes in upper and lower Ti nanodisks, implying that electromagnetic energy is lost in the structure. The distributions of surface current at each resonant wavelength for the lower and upper layer are plotted in Figs. 6(d)–(f) and 6(g)–(i), respectively. Unlike with the initial structure, surface current distributions exhibit the same resonance characteristics. As shown in Figs. 6(d)–(i), for both lower and upper layer, the surface currents mainly distribute in the left and right interface between metal and embedded insulator layer, which indicates that the mode matching between the MIM cavity and embedded layer occurs and a new resonant mode is generated. Moreover, we also can observe that the incident waves can excite the

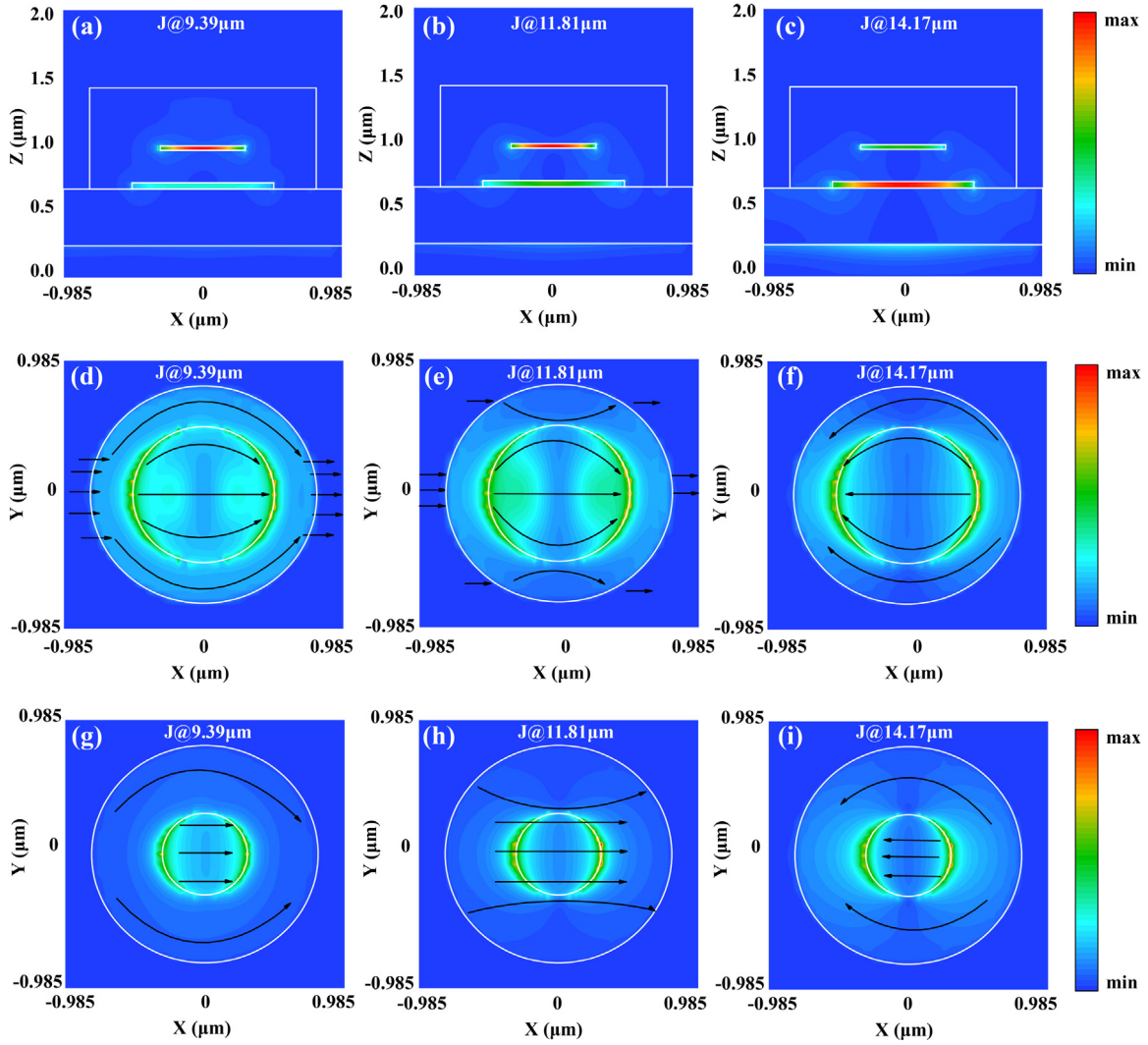

Fig. 6. (a)–(c) current density distributions (colour bar in the x-z plane) at different resonant wavelengths. (d)–(f) Surface current distributions in lower metamaterial layer (colour bar in the x-y plane) at different resonant wavelengths. (g)–(i) Surface current distributions in upper metamaterial layer (colour bar in the x-y plane) at different resonant wavelengths.

parallel currents between lower and upper metamaterial layer at each resonant wavelength, implying the induced parallel electric dipoles play a main role in broadband absorption.

Similar results of field distribution are presented in Fig. 7 for the modified embedded structure. The differences and similarities between the absorption mechanisms of these two structures are obvious from those figures. For the modified embedded structure, as observed in Figs. 7(a)–(c), electric field is not only intensively enhanced around of both upper and lower Ti nanodisks, but also localized around the bulk Ge insulator disks between the adjacent unit cells. Judging from the electric field distribution, the resonance is the electric dipole resonances excited on the nanodisks, thus coupling the energy of light into the slot between the Ti nanodisk corners and the surrounding Ge insulator [36]. The magnetic field distributions of the x-z plane are further presented in Figs. 7(d)–(f). Overall, the magnetic field magnitude is greatly enhanced in different dielectric layers that are close to the metal layers at resonant frequencies, which indicates that the resonances are created within the insulator cavity separated by the upper and lower metamaterial ring layers. Significant magnetic field enhancement at the cavity signifies that a new dielectric-loaded metal waveguide mode is coupled into the cavity. The combination of embedded insulator layer and metallic nanodisks is often known as dielectric-loaded surface plasmon polaritons waveguide [37]. Therefore, the hybrid embedded cavity mode originates from the combination of dielectric-loaded surface plasmon polaritons waveguide and cavity modes, which further promotes the trapping and absorption of incident light. The magnetic field shows the similar field profile at each resonant wavelength, which indicates that the embedded cavity modes dominate the absorption. It is worth noting that the resonances also originate from the hybridization between the embedded cavity modes in the upper and lower cavities.

3.3. Effects of geometry and oblique incidences on absorbance of metamaterial absorbers

We also carry out a similar numerical analysis of geometry effects for the modified embedded structure. The influence of the thickness of insulator spacer at different levels (d_{21}, d_{22} and d_{23}), the radius of the lower and upper Ti nanodisk (r_{21} and r_{22}) and the radius of the bulk Ge nanodisk (r_{23}) on the absorption spectra is shown in Fig. 8. Overall, as depicted in Figs. 8(a)–(c), nearly all the absorption peaks produced by the hybrid embedded cavity modes undergo a redshift with growing thickness of the insulator. This phenomena is well explained by the interference theory that the insulator thickness is a key factor to control the absorption maxima and the reflection coefficient of the metamaterial absorbers [38]. The absorption peak frequencies are the result of multiple factors which involve the resonant frequencies

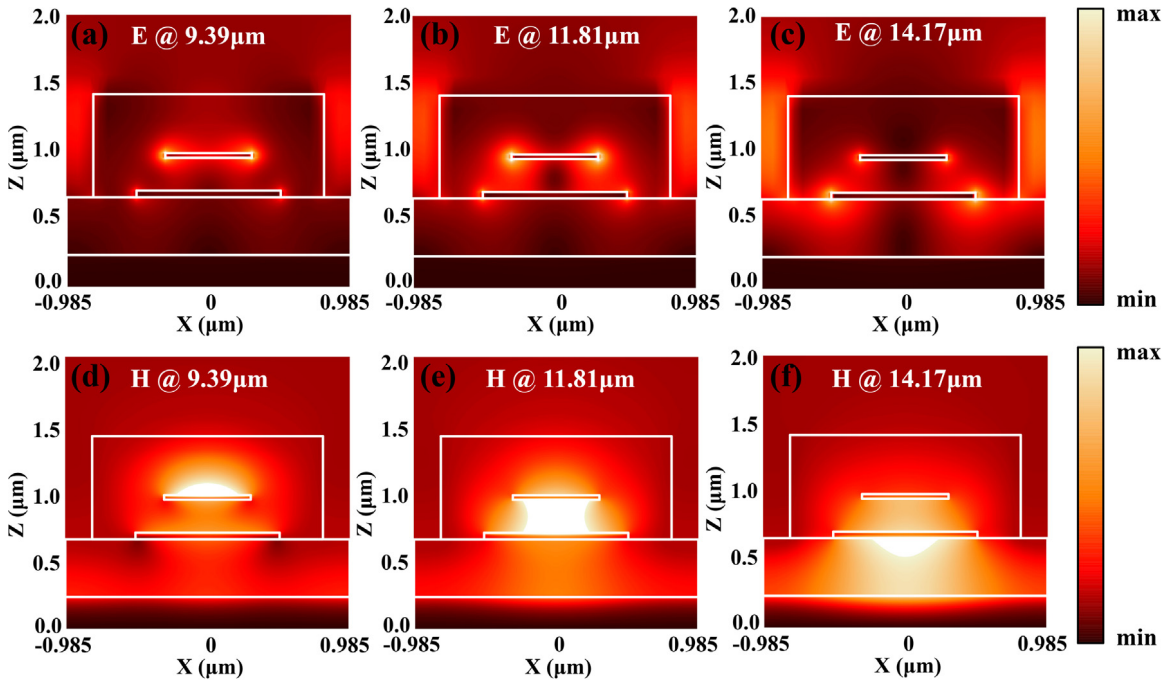

Fig. 7. (a)–(c) Electric field $|E|$ distributions (colour bar in the x-z plane) at different resonant wavelengths. (d)–(f) Magnetic field $|M|$ distributions (colour bar in the x-z plane) at different resonant wavelengths.

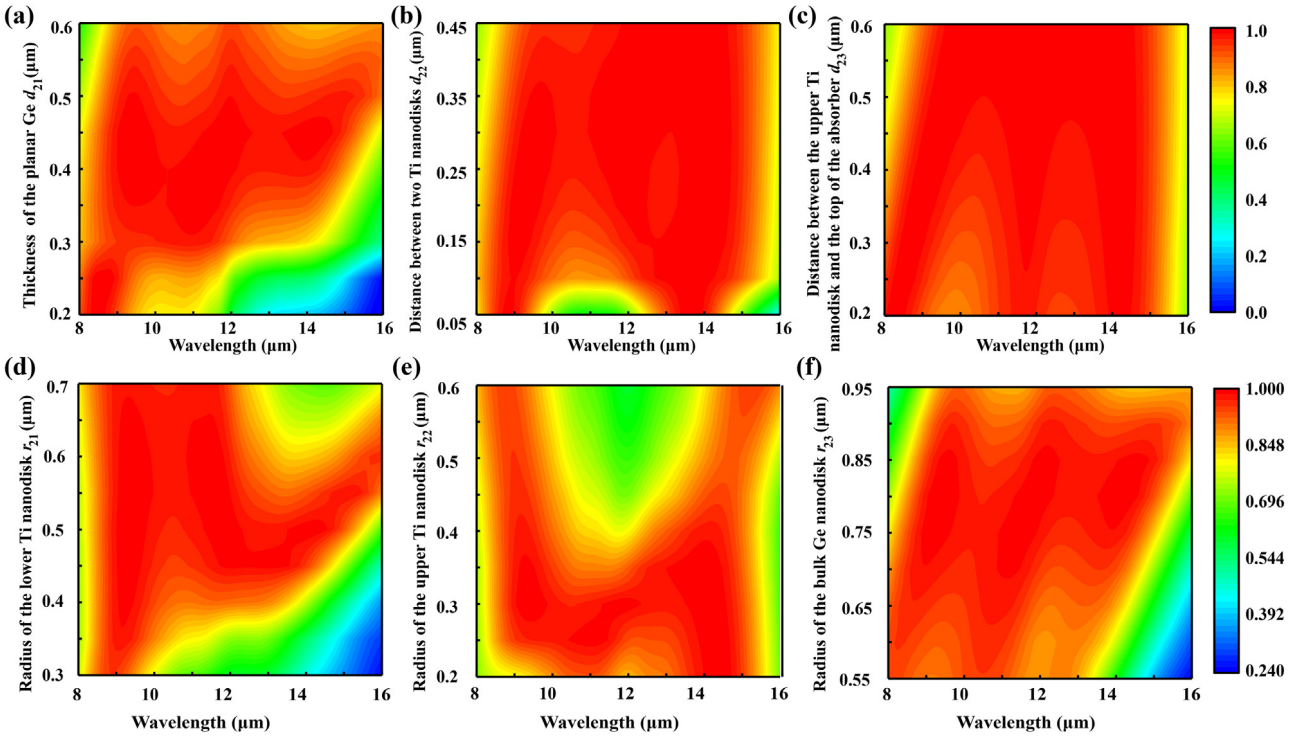

Fig. 8. Demonstration of the geometric effects on the absorption performances: (a) the thickness of the planar Ge layer (d_{21}), (b) the face-to-face distance between the two patterned metal layers (d_{22}), (c) the distance between the upper Ti nanodisk and the top of the bulk Ge nanodisk (d_{23}), (d)–(e) the radius of the lower and upper Ti nanodisk r_{21} and r_{22}, (f) the radius of the bulk Ge nanodisk (r_{23}).

of the metamaterial absorbers and a frequency shift determined by the phase delay in the insulator layer. Therefore, absorption peaks and the corresponding hybrid embedded cavity modes are slightly red-shifted with the increase of the insulator thickness. Specifically, the thickness of the Ge planar is mostly depended on embedded cavity modes at the insulator substrate. Thus, all of the absorption peaks are affected by the variation of d_{21}. Analogously, the variation of d_{22} and d_{23}determines the resonances created within different cavities, which in turn tunes the resonant wavelength. Specially, we noticed the function of the top insulator cavity differed from previous research. We can observe from Fig. 8(c) that as the thickness t_3 increases, the structure shows an intensive resonance mode, resulting in high average absorptivity and well merged absorption peaks. The top insulator creates a transition between the free space and embedded metamaterial ring, which

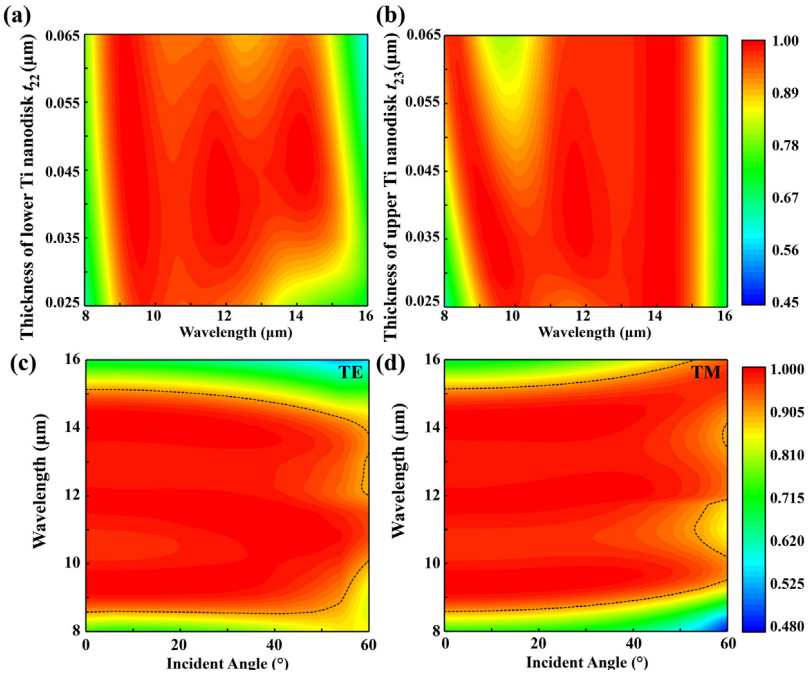

Fig. 9. Absorption varying with Ti nanodisks thickness and oblique incidences in the absorber structure: (a)–(b) the thickness of the lower Ti nanodisk (t_{22}) and upper Ti nanodisk (t_{23}), (c)–(d) the incident angle for TE-polarized and TM-polarized, the dashed line represents the contour line with an absorption magnitude of 90%.

provides a better impedance matching condition between air and the metamaterial absorber. On the other hand, as shown in Figs. 8(d)–(e), the embedded cavity modes exhibit high sensitivity to the variation of the radius of nano-disks, which is analogous with cavity modes based on the constructive interference of coupled surface plasmons. As to the impact of the radius of the bulk Ge nanodisk, it is seen from Fig. 8(f) that the three absorption peaks undergo a uniform redshift and the absorptivity remains substantially unchanged with increasing radius of the bulk Ge nanodisk. This indicates that the wavelength-selective metamaterial absorber is realized by controlling the radius of the bulk insulator nanodisk.

It is obviously from the comparison between two structures reported in this paper that the embedded metamaterial ring layers play an important role in the absorption performance of the metamaterial absorber. To better understand the absorption mechanism behind the embedded structure, we selected the lower three layers which comprise the bottom Ti functional layer, the planar Ge substrate, and the embedded metal–insulator ring to research. In this condition, due to the identical components, except the embedded metal–insulator ring, the equivalent medium can be regard as a collection of the air, the bottom Ti functional layer, and the planar Ge substrate. Since the bottom Ti functional layer is thick enough to block all the transmission in working waveband, the transmission (T) and reflection (R) coefficients can be obtained from the following equations [39]:

$$R = \frac{\eta - \eta_e}{\eta + \eta_e} \tag{3}$$

$$T = \frac{2\eta}{\eta + \eta_e} \tag{4}$$

$$\eta \simeq (1+j)\sqrt{\frac{\omega\mu}{2\sigma}} = (1+j)\frac{1}{\sigma\delta_s} \tag{5}$$

Where η and η_e are the intrinsic impedances of the embedded metal–insulator ring and equivalent medium, ω, μ and σ are the angular frequency, magnetic permeability and electrical conductivity of the embedded metal–insulator ring, respectively. The equations show that the absorption performance of the embedded metamaterial absorber is closely related to the thickness of the embedded metal–insulator ring. The influences of the Ti nanodisks thicknesses (t_{22} and t_{23}) on absorption spectra are shown in Figs. 9(a) and 9(b). We note that embedded metamaterial absorber professes great sensitivity to the thickness of the Ti nanodisks. As increase with t_{22} and t_{23}, the absorption peaks undergo a blueshift and absorptivity fluctuation. It is in agreement with the results obtained from theoretical analysis.

According to the symmetries of the structure, we additionally investigated the effects of the polarization and angle on absorption. Absorptions with oblique incidences for both TE-polarized (x-polarized) and TM-polarized (y-polarized) waves are shown in Figs. 9(c) and 9(d), respectively. The incident angle is swept by a step of 6° from 0° to 60°. One can see that, with incident angles up to 45°, the average absorption is almost unchanged for both polarizations. For larger incident angles, the structure takes on different behaviours for TE-polarized and TM-polarized waves. Specifically, in case of TE-polarized wave, the absorptivity and bandwidth gradually decrease for larger incident angles. This is owing to that the horizontal component of the incident magnetic field decreases with an increase in θ, resulting in a decrease in the strength of the coupling and the absorption. Regarding TM-polarized wave, the figure shows that the bandwidth at the longer wavelengths is slightly broaden and gains red shift. The dashed line in Figs. 9(c) and 9(d) represents 90% absorption, which indicates excellent absorption performance for both TM and TE polarizations.

4. Conclusion

In summary, we have proposed a novel ultra-broadband, polarization-independent, and wide-angle metamaterial absorber based on embedded metal–insulator metamaterial in the LWIR band. The proposed structure exhibits more than 94% absorbance in the interval from 8.00 μm to 16.00 μm; and more than 95% absorbance over the whole LWIR band (8-14 μm), which is superior than the initial traditional MIM structure (absorption greater than 90% from 8.10-14.33 μm) and similar kinds of metamaterial absorber based on noble metal. In addition, a nearly perfect absorbance (more than 99%) is obtained in the 11.22–12.46 μm and 13.26–14.59 μm wavebands. The outstanding absorption performance of the metamaterial absorber mostly lies on the excitation of multiple embedded cavity modes generated by the combination of dielectric-loaded surface plasmon polaritons waveguide and cavity modes. The superiority of the embedded structure is numerically

investigated by comparing the physical mechanism and the geometry effects of the two metamaterial absorbers. Meanwhile, by varying related geometry parameters, the resonant wavelength and operating bandwidth can be adjusted flexibly to achieve the wavelength-selective metamaterial absorber. This work provides the reference for the design of tunable broadband LWIR absorbers. It is manifest that this design method can be extended to medium wavelength infrared band, very long-wavelength infrared, terahertz or visible regimes. Thus, we believe our designed absorber with MEMS-COMOS technology compatibility has many potential applications in thermal emitters, microbolometer, solar-energy harvesting, and chemical sensing applications.

Acknowledgements

This study was supported by the National Natural Science Foundation of China (Grant Numbers 61735018, 61376122 and 61805242), Excellent Member of Youth Innovation Promotion Association CAS (Grant Numbers. 2014193), Scientific and Technological Development Project of Jilin province (Grant Numbers. 20170204077GX), Leading Talents and Team Project of Scientific and Technological Innovation for Young and Middle-aged Groups in Jilin Province (20190101012JH), Independent fund of State Kay Laboratory of Applied Optics, Overseas Students Science and Technology Innovation and Entrepreneurship Projects of Jilin province, Project of CIOMP-Duke Collaborative Research, Project of CIOMP-Fudan University Collaborative Research.

References

[1] T. Maier, H. Brueckl, Multispectral microbolometers for the mid-infrared, Opt. Lett. 35 (22) (2010) 3766–3768.
[2] J.-Y. Jung, K. Song, J.-H. Choi, J. Lee, D.-G. Choi, J.-H. Jeong, D.P. Neikirk, Infrared broadband metasurface absorber for reducing the thermal mass of a microbolometer, Sci. Rep. 7 (1) (2017) 430.
[3] S. Haxha, F. AbdelMalek, F. Ouerghi, M.D.B. Charlton, A. Aggoun, X. Fang, Metamaterial superlenses operating at visible wavelength for imaging applications, Sci. Rep. 8 (2018) 16119.
[4] Y. Gong, Z. Wang, K. Li, L. Uggalla, J. Huang, N. Copner, Y. Zhou, D. Qiao, J. Zhu, Highly efficient and broadband mid-infrared metamaterial thermal emitter for optical gas sensing, Opt. Lett. 42 (21) (2017) 4537–4540.
[5] Z. Li, L. Stan, D.A. Czaplewski, X. Yang, J. Gao, Wavelength-selective mid-infrared metamaterial absorbers with multiple tungsten cross resonators, Opt. Lett. 26 (5) (2018) 5616–5631.
[6] A.K. Azad, W.J. Kort-Kamp, M. Sykora, N.R. Weisse-Bernstein, T.S. Luk, A.J. Taylor, D.A. Dalvit, H.T. Chen, Metasurface broadband solar absorber, Sci. Rep. 6 (2016) 20347.
[7] S. Han, J.-H. Shin, P.-H. Jung, H. Lee, B.J. Lee, Broadband solar thermal absorber based on optical metamaterials for high-temperature applications, Adv. Opt. Mater. 4 (8) (2016) 1265–1273.
[8] F.O. Alkurt, O. Altintas, A. Atci, M. Bakir, E. Unal, O. Akgol, K. Delihacioglu, M. Karaaslan, C. Sabah, Antenna-based microwave absorber for imaging in the frequencies of 1.8, 2.45, and 5.8 GHz, Opt. Eng. 57 (11) (2018) 113102.
[9] F.O. Alkurt, O. Altintas, M. Bakir, A. Tamer, F. Karadage, M. Bagmanci, M. Karaaslan, E. Unal, O. Akgol, Octagonal shaped metamaterial absorber based energy harvester, Mater. Sci. 24 (3) (2018) 2029–7289.
[10] C. Wu, A.B. Khanikaev, R. Adato, N. Arju, A.A. Yanik, H. Altug, G. Shvets, Fano-resonant asymmetric metamaterials for ultrasensitive spectroscopy and identification of molecular monolayers, Nature Mater. 11 (1) (2011) 69–75.
[11] N.I. Landy, S. Sajuyigbe, J.J. Mock, D.R. Smith, W.J. Padilla, Perfect metamaterial absorber, Phys. Rev. Lett. 100 (20) (2008) 207402.
[12] J. Grant, Y. Ma, S. Saha, A. Khalid, D.R. Cumming, Polarization insensitive, broadband terahertz metamaterial absorber, Opt. Lett. 17 (36) (2011) 3476–3478.
[13] P. Zhu, L.J. Guo, High performance broadband absorber in the visible band by engineered dispersion and geometry of a metal–dielectric-metal stack, Appl. Phys. Lett. 101 (24) (2012) 241116.
[14] P. Feng, W.-D. Li, W. Zhang, Dispersion engineering of plasmonic nanocomposite for ultrathin broadband optical absorber, Opt. Express 23 (3) (2015) 2328–2338.
[15] S.A. Dereshgi, Z. Sisman, K. Topalli, A.K. Okyay, Plasmonically enhanced metal–insulator multistacked photodetectors with separate absorption and collection junctions for near-infrared applications, Sci. Rep. 7 (2017) 42349.
[16] T. Maier, H. Bruckl, Wavelength-tunable microbolometers with metamaterial absorbers, Opt. Lett. 19 (34) (2009) 3012–3014.
[17] T. Maier, H. Bruckl, Multispectral microbolometers for the midinfrared, Opt. Lett. 22 (35) (2010) 3766–3768.
[18] W. Ma, D. Jia, Y. Wen, X. Yu, Y. Feng, Y. Zhao, Diode-based microbolometer with performance enhanced by broadband metamaterial absorber, Opt. Lett. 13 (41) (2016) 2974–2977.
[19] X. Liu, T. Tyler, T. Starr, A. Starr, N. Jokerst, W. Padilla, Taming the blackbody with infrared metamaterials as selective thermal emitters, Phys. Rev. Lett. 107 (2011) 045901.
[20] W. Ma, Y. Wen, X. Yu, Broadband metamaterial absorber at midinfrared using multiplexed cross resonators, Opt. Express 21 (2013) 30724–30730.
[21] B. Adomanis, C. Watts, M. Koirala, X. Liu, T. Tyler, K. West, T. Starr, J. Bringuier, A. Starr, N. Jokerst, W. Padilla, Bi-layer metamaterials as fully functional near-perfect infrared absorbers, Appl. Phys. Lett. 107 (2015) 021107.
[22] W. Guo, Y. Liu, T. Han, Ultra-broadband infrared metasurface absorber, Opt. Lett. 35 (24) (2016) 20586–20592.
[23] S. Dai, D. Zhao, Q. Li, M. Qiu, Double-sided polarization-independent plasmonic absorber at near-infrared region, Opt. Express 11 (21) (2013) 13125–13133.
[24] A. Hubarevich, A. Kukhta, H.V. Demir, X. Sun, H. Wang, Ultra-thin broadband nanostructured insulator–metalinsulator–metal plasmonic light absorber, Opt. Express 8 (23) (2015) 9753–9761.
[25] S. Wu, Y. Gu, Y. Ye, H. Ye, L. Chen, Omnidirectional broadband metasurface absorber operating in visible to near-infrared regime, Opt. Express 17 (26) (2018) 21479–21489.
[26] M.R. Soheilifar, R.A. Sadeghzadeh, Design, Fabrication and characterization of stacked layers planar broadband metamaterial absorber at microwave frequency, Int. J. Electron. Commun. 69 (2015) 126–132.
[27] X. Ling, Z. Xiao, X. Zheng, Broadband near-infrared metamaterial absorbers utilizing highly lossy metals, Sci. Rep. 6 (2016) 39445.
[28] K. Üstün, G. Turhan-Sayan, A three-dimensional broadband infrared metamaterial absorber based on the plasmonic and dipole resonance responses, Plasmonics 13 (1) (2018) 175–180.
[29] E.D. Palik, Handbook of Optical Constants of Solids 3, Academic press, New York, 1998.
[30] L. Lei, S.Ly, H. Huang, K. Tao, P. Xu, Ultra-broadband absorber from visible to near-infrared using plasmonic metamaterial, Opt. Express 5 (26) (2018) 5686–5693.
[31] H.-T. Chen, Interference theory of metamaterial perfect absorbers, Opt. Express 7 (20) (2012) 7165–7172.
[32] R. Filter, J. Qi, C. Rockstuhl, F. Lederer, Circular optical nanoantennas: an analytical theory, Phys. Rev. B 85 (2012) 125429.
[33] F. Minkowski, F. Wang, A. Chakrabarty, Q.-H. Wei, Resonant cavity modes of circular plasmonic patch nanoantennas, Appl. Phys. Lett. 104 (2014) 021111.
[34] A. Ghobadi, S.A. Dereshgi, H. Hajian, B. Bozok, B. Butun, E. Ozbay, Ultra-broadband, wide angle absorber utilizing metal insulator multilayers stack with a multi-thickness metal surface texture, Sci. Rep. 7 (1) (2017) 4755.
[35] M. Karaaslan, M. Bağmancı, E. Ünal, O. Akgol, C. Sabah, Microwave energy harvesting based on metamaterial absorbers with multi-layered square split rings for wireless communications, Opt. Commun. 392 (2017) 31–38.
[36] F. Ding, J. Dai, Y. Chen, J. Zhu, Y. Jin, S.-I. Bozhevolnyi, Broadband near-infrared metamaterial absorbers utilizing highly lossy metals, Sci. Rep. 6 (2016) 39445.
[37] T. Holmgaard, S.I. Bozhevolnyi, Theoretical analysis of dielectric-loaded surface plasmon-polariton waveguides, Phys. Rev. B 75 (24) (2007) 245405.
[38] G. Duan, J. Schalch, X. Zhao, J. Zhang, R.D. Averitt, X. Zhang, Analysis of the thickness dependence of metamaterial absorbers at terahertz frequencies, Opt. Express 26 (3) (2018) 2242–2251.
[39] L. Hai, V. Qui, N. Tung, T. Huynh, N. Dung, N. Binh, L. Tuyen, V. Lam, Conductive polymer for ultra-broadband, wide-angle, and polarization-insensitive metamaterial perfect absorber, Opt. Express. 25 (26) (2018) 33253–33262.